Electronic Supplementary Information

Mechanism of Creation and Destruction of Oxygen Interstitial Atoms by Nonpolar Zinc Oxide($10\bar{1}0$) Surfaces

Heonjae Jeong[a], Ming Li[b], Jingtian Kuang[b], Elif Ertekin[a], and Edmund G. Seebauer*[b]

[a]Department of Mechanical Science and Engineering, University of Illinois at Urbana-Champaign, Urbana, Illinois 61801, USA

[b]Department of Chemical and Biomolecular Engineering, University of Illinois at Urbana-Champaign, Urbana, Illinois 61801, USA

*Corresponding author: Edmund G. Seebauer

Table of Contents

1. Shallow-slope profiles

After subtraction of the natural-abundance baseline from raw isotopic profiles, small but nonzero slopes become evident as shown in the examples below.

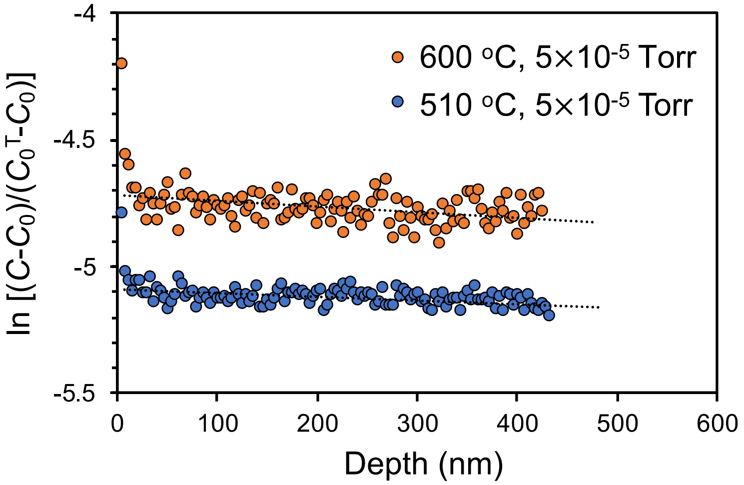

Figure S1. Normalized ^{18}O concentration profiles for nonpolar ZnO($10\bar{1}0$) annealed at T = 510 °C and (blue) and 600 °C (orange) at P_{O_2}= 5 × 10^{-5} Torr.

2. Description and comparison of mesoscale modeling approaches

2.1. Classical equilibrium model

2.1.1. Background

If T and P_{O_2} are maintained between the equilibration and diffusion steps in self-diffusion experiments, the isotopic label moves in the absence of a spatial gradient in chemical composition. The tracer diffusivity[1] describes the label's resulting profile. If T and P_{O_2} are changed so that gradients in defect populations arise, the chemical diffusivity[2] describes the resulting profile. In studies of chemical elements that do not readily gasify or adsorb under laboratory conditions, isotopic heterojunctions serve purposes similar to gas exchange experiments.[3]

Classical formalisms for tracer diffusivities assume global equilibrium throughout the solid,[4] while those for chemical diffusivities assume local equilibrium[2,5] manifested in a thermodynamic factor. However, tracer or chemical diffusivities represent composite quantities from which deconvolution of site-to-site hopping diffusivities D_{hop} from thermodynamic terms can be difficult. More importantly, in some semiconductors the assumption of either global or local equilibrium is questionable. In ZnO and TiO_2, for example, O vacancies were long assumed to dominate diffusive behavior of oxygen even under conditions where first-principles calculations pointed to O_i as the most stable species thermodynamically.[6–12] High barriers for generating O_i via bulk pathways rendered those alternatives kinetically inaccessible during practical laboratory time scales. Recent work has partly circumvented this problem by employing clean surfaces to generate interstitials via lower-energy pathways that are experimentally accessible.[13–15] However, sequestration and release of these interstitials by slowly evolving extended defects[16–18] impedes the approach to true equilibrium, thereby complicating the interpretation of the fitted diffusivities.

2.1.2. Mathematical implementation

In the equilibrium approximation, evolution of the concentration C of isotopic label in a tracer experiment as a function of time t and depth x obeys Fick's second law:

$$\frac{\partial C}{\partial t} = D_{tr}\frac{\partial^2 C}{\partial x^2} \qquad \text{(S1)},$$

where D_{tr} denotes the tracer diffusivity. A convenient solution that circumvents use of a surface exchange coefficient K results by solving the diffusion equation in terms of a net injection flux F of isotopic label that is assumed constant. At the surface (x= 0), the boundary condition becomes

$$F = -D_{tr}\left.\frac{\partial C}{\partial x}\right|_{x=0} \qquad \text{(S2)}.$$

With an initial label concentration C_0 distributed uniformly throughout the semi-infinite bulk (typically at the natural-abundance level), the concentration in the deep bulk remains at C_0 according to the boundary condition

$$C(x \to \infty, t) = C_0 \qquad \text{(S3)}$$

The solution to these equations is[19,20]

$$C - C_0 = 2F\left(\frac{t}{\pi D_{tr}}\right)^{\frac{1}{2}}\exp\left(-\frac{x^2}{4D_{tr}t}\right) - \frac{Fx}{D_{tr}}erfc\left(\frac{x}{2\sqrt{D_{tr}t}}\right) \qquad \text{(S4)}.$$

Near the surface in the limit $x \to 0$, the slope M of this profile reduces to

$$M = -\frac{F}{D_{tr}} \qquad \text{(S5)},$$

and the intercept B is given by

$$B = 2F\left(\frac{t}{\pi D_{tr}}\right)^{1/2} \qquad \text{(S6)}.$$

Rearrangement of these expressions leads to the following expressions for F and D_{tr}:

$$F = -\frac{\pi B^2}{4Mt} \qquad \text{(S7),}$$

and

$$D_{tr} = \frac{\pi B^2}{4M^2 t} \qquad \text{(S8),}$$

Propagation of small uncertainties ΔM in the slope and ΔB in the intercept manifest in F and D_{tr} according to

$$\frac{\Delta F}{F} = -\frac{\Delta M}{M} + 2\frac{\Delta B}{B} \qquad \text{(S9),}$$

and

$$\frac{\Delta D_{tr}}{D_{tr}} = -2\frac{\Delta M}{M} + 2\frac{\Delta B}{B} \qquad \text{(S10).}$$

Thus, fractional uncertainties in the intercept propagate equally into the two composite parameters, but fractional uncertainties in the slope propagate more strongly into D_{tr} than into F.

Eq. (S2) presupposes D_{tr} is the mathematical product of D_{hop} and a mole fraction of mobile species – $\mathrm{O_i}$ in the present case. When the crystal lattice serves as the sequestration site for the mobile species, as is typically the case for oxygen vacancies $\mathrm{V_O}$, the mole fraction consists of the concentration of $\mathrm{V_O}$ divided by the concentration of lattice sites containing O.

Extrinsic impurities or extended defects of concentration [S] serve as the primary sequestration sites for $\mathrm{O_i}$ in ZnO, so the mole fraction requires a different definition. Local steady state is assumed to exist between $\mathrm{O_i}$ and S, with most $\mathrm{O_i}$ residing in complexed form at concentration $[\mathrm{S_C}]$. The mole fraction contained within D_{tr} should therefore be normalized by $\mathrm{S_C}$ according to $[\mathrm{O_i}]/[\mathrm{S_C}]$.

This phenomenon, coupled with the statistical factor modifying D_{hop} described in the main text, lead to the following expression for D_{tr}:

$$D_{tr} = \frac{[O_i]}{[S_C]} \frac{[^{18}O_i]}{[^{16}O_i] + [^{18}O_i]} D_{hop} \tag{S11}$$

This definition permits computation of D_{tr} from the microkinetic model, and enables direct comparison with corresponding values of D_{tr} from the classical equilibrium model.

2.2. Hybrid mesoscale model in short-time limit

2.2.1. Background

Hybrid approaches exist between classical models and microkinetic simulators. Example hybrids have successfully described evolution of delta-function dopant profiles in Si,[21] step-function isotope profiles in Si,[22] and isotopic self-diffusion in TiO_2.[23] These approaches typically work within "short-time" asymptotic limits wherein the mobile species undergoes a single sequestration event during a self-diffusion experiment. Profile fitting yields composite parameters, but requires relatively few assumptions that do not necessarily include equilibrium. Hybrid models can yield physical insights that remain unavailable at the classical or microkinetic endpoints.

A hybrid model applied to the present dataset entails solution of two continuum differential equations describing the spatial and temporal evolution of mobile and immobile forms of the isotopic label.[23] In a short-time asymptotic limit, mobile O_i diffuses until sequestration, remaining there for the duration of the experiment. Local steady state is not required. The profile slope plotted on a semi-logarithmic scale yields the mean diffusion length λ, while the intercept yields F. The parameters may be combined to yield the effective diffusivity $D_{eff} = F\lambda^2$.

2.2.2. Numerical implementation

The short-time approximation predicts a profile wherein the concentration of sequestered label C varies with time t and depth x according to

$$ln\left(\frac{C - C_0}{C_0^T - C_0}\right) = ln\left(\frac{F}{\lambda(C_0^T - C_0)}t\right) - \frac{x}{\lambda} \qquad \text{(S12)},$$

where C_0 denotes the initial label concentration and C_0^{T} denotes the total concentration of sequestration sites. The slope of the profile equals $-1/\lambda$, and the intercept equals ln($^{Ft}/(\lambda(C_0^T - C_0))$). In oxides such as rutile TiO_2 wherein extended defects of concentration [E] (distinguished from complexation sites of concentration [S]) serve as the sole sequestration sites, λ obeys[18]

$$\lambda = \sqrt{\frac{1}{4\pi a[E]}} \qquad \text{(S13)},$$

where a represents a capture radius.

The effective diffusivity[24] D_{eff} may be computed by

$$D_{eff} = \frac{F\lambda}{[C_0^T - C_0^{18}]} \qquad \text{(S14)}.$$

Physically, D_{eff} is equivalent to D_{tr}. However, the distinct different notation emphasizes that numerical values for D_{tr} originate from assumptions and procedures differing significantly from those for D_{eff}, and are only loosely comparable.

2.2.3. Results and discussion

Application of the short-time formalism to the present data set results in in Figures S2 and S3 below. Close consideration of the numbers reveals a self-consistency problem. With a capture radius of 2×10^{-8} cm,[25] the values of λ near 10^4 nm imply $[E] \approx 4\times10^{12}$ cm^{-3}. With a lattice oxygen concentration of 6.38×10^{22} cm^{-3}, this concentration corresponds to an extended defect mole fraction of about 10^{-10}. Even with extended defects capable of holding several million label atoms, this mole fraction seems too low to cohere with measured label concentrations near 1%.

Furthermore, accretion of O_i onto such extended defects such as edge or screw dislocations would presumably require concurrent accretion of zinc interstitial atoms Zn_i in a stoichiometric proportion, as occurs for O_i and Ti interstitials in TiO_2.[26,27] Because Zn vacancies V_{Zn} are thermodynamically favored over Zn_i under present experimental conditions,[7,9] such a scenario seems unlikely. Thus the classical thermodynamic model described above with small-cluster sequestration sites offers a better framework for profile analysis.

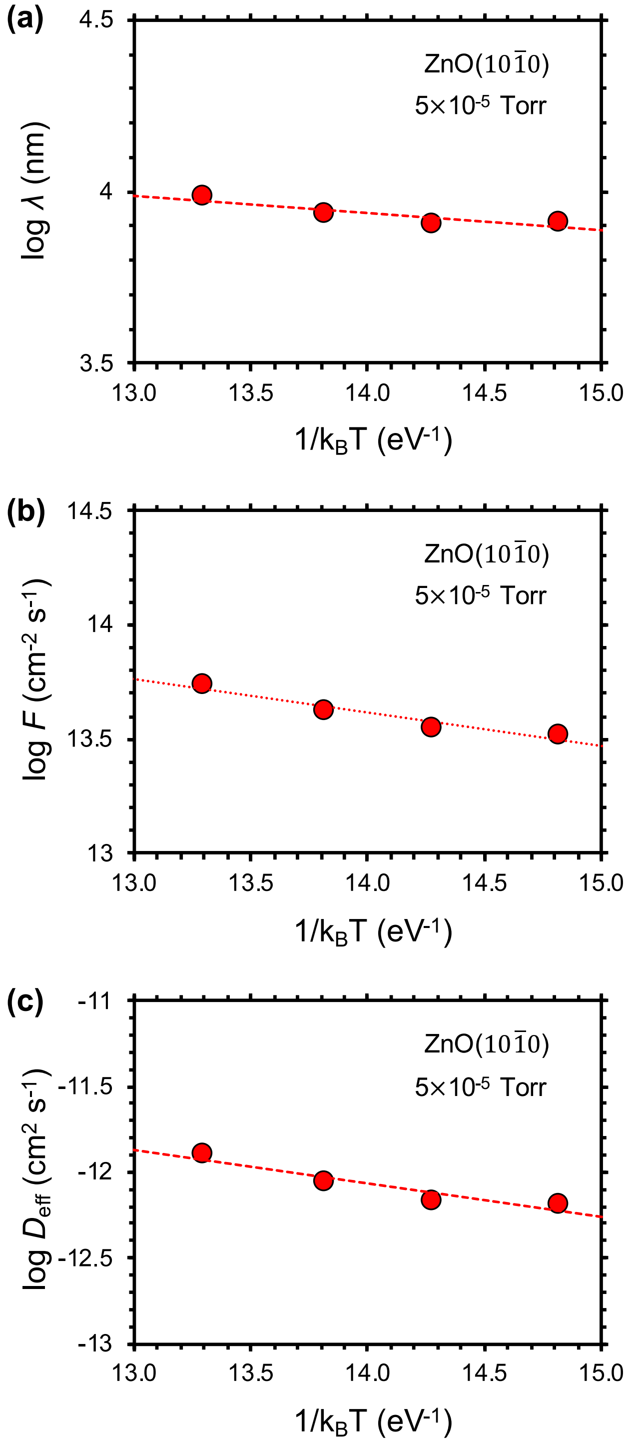

Figure S2. Arrhenius plot of (a) mean diffusion length λ, (b) net injection flux F, and (c) effective diffusivity D_{eff} for the short-time hybrid model at P_{O_2}= 5 × 10^{-5} Torr. Symbols represent specific profiles, while the dashed line represents a least-squares fit.

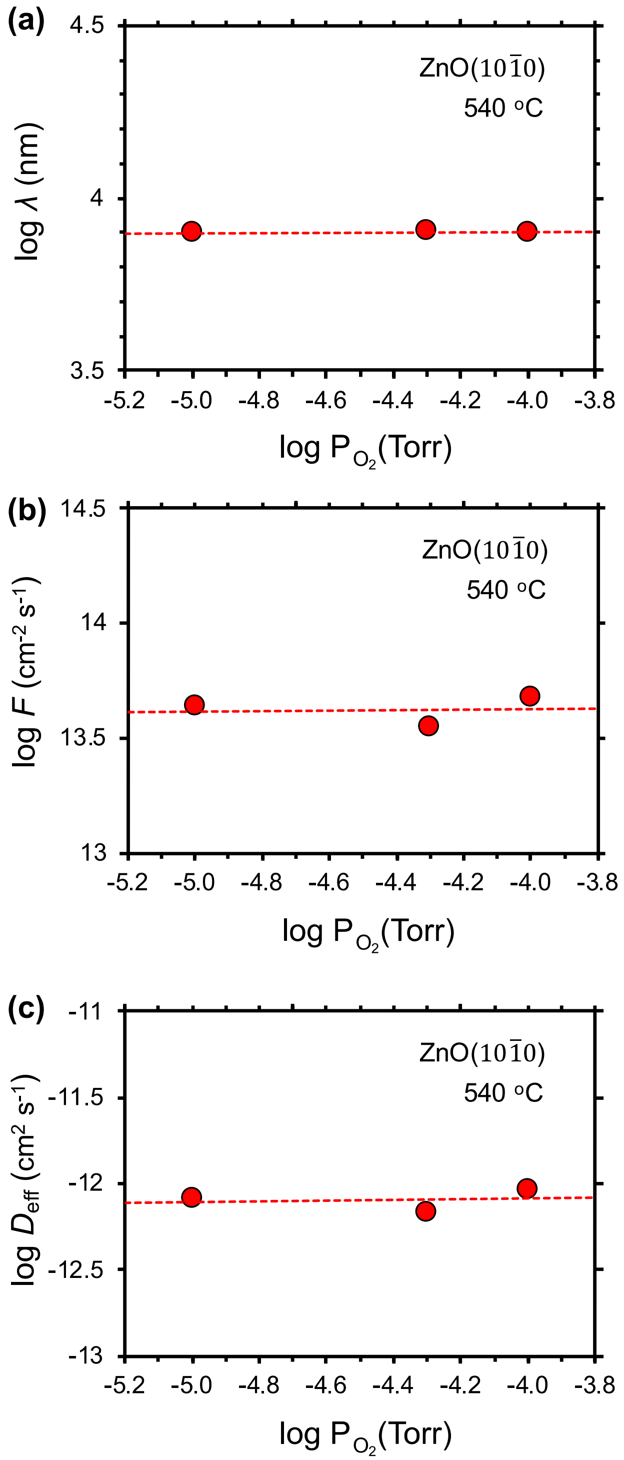

Figure S3. Oxygen partial pressure dependence of (a) mean diffusion length λ, (b) net injection flux F, and (c) effective diffusivity D_{eff} for the short-time hybrid model at T = 540 °C. Symbols represent specific profiles, while the dashed line represents a least-squares fit.

2.3. Microkinetic modeling

2.3.1. Coverage of injectable O assuming [O$_i$] at equilibrium

For the microkinetic model detailed in the main text, Figure S4(a) shows the surface coverage θ of injectable O species as a function of T and P_{O_2} determined by[24]

$$\theta = \frac{3D_{hop}S_0[O_i]_{x=0}}{n_{sat}l\nu_{inj}e^{-E_{inj}/k_BT} + 3D_{hop}S_0[O_i]_{x=0}}$$

$$= \frac{1}{\frac{n_{sat}l\nu_{inj}e^{-E_{inj}/k_BT}}{3D_{hop}S_0[O_i]_{x=0}} + 1} \qquad \text{(S15)},$$

where S_0 denotes the zero-coverage annihilation probability of O$_i$, $[O_i]_{x=0}$ is the total concentration of O$_i$ at $x = 0$, n_{sat} is the saturation concentration of injection sites, l is the hopping length on the order of the lattice spacing (2.68×10^{-8} cm),[24] ν_{inj} is the injection pre-exponential factor, and E_{inj} is the injection activation barrier. The coverage increases as both T and P_{O_2} increase, although θ remains well below unity for the entire range of conditions shown (400–1600 °C and 10^{-10}–760 Torr). In the range of conditions directly measured in the experiments (T = 510 – 600 °C and $P_{O_2} = 10^{-5} - 10^{-4}$ Torr), θ spans 1.3×10^{-7} to 4.7×10^{-7}. Note, however, that all this behavior assumes that both θ and [O$_i$] take on equilibrium values.

Figure S4(b) shows an Arrhenius plot for the elementary-step injection and annihilation rates for ^{18}O computed from the microkinetic model according to Eqs. (S16) and (S17) shown below, together with $F = r_{\mathrm{inj}} - r_{\mathrm{ann}}$, where

$$r_{inj} = \nu_{inj}e^{-E_{inj}/k_BT} n_{sat}\theta \qquad \text{(S16)},$$

$$r_{ann} = \frac{3D_{hop}S_0}{l}(1-\theta)[O_i]_{x=0} \qquad \text{(S17)}.$$

The figure shows that $r_{\text{inj}} >> r_{\text{ann}}$ for ^{18}O, so that $F \approx r_{\text{inj}}$. Note that the assumption of chemical equilibrium requires that $r_{\text{inj}} = r_{\text{ann}}$ when summing both isotopes ^{16}O + ^{18}O. An obvious corollary is that $r_{\text{inj}} << r_{\text{ann}}$ for ^{16}O, which was verified in the simulations (not shown in Figure S4(b)).

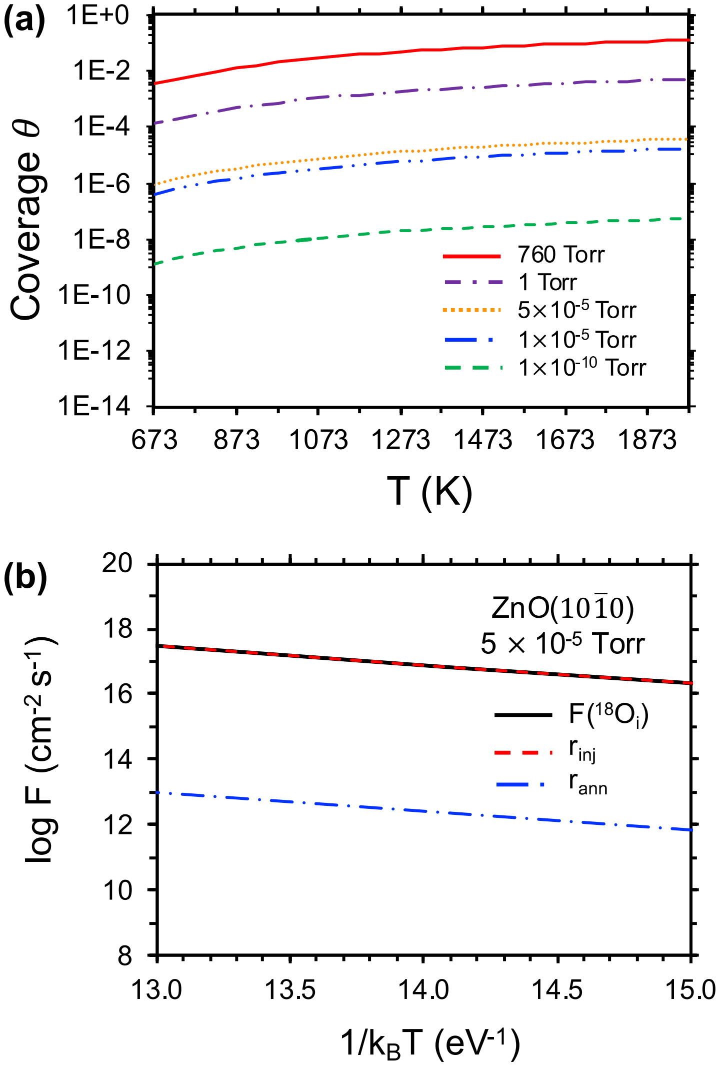

Figure S4. (a) Coverage of injectable O as a function of T and P_{O_2}. (b) Arrhenius plot of net injection flux F of ^{18}O$_i$ (black solid) together with rates of elementary-step injection r_{inj} (red dashed) and annihilation r_{ann} (blue dashed-dot). F closely follows r_{inj}.

Because this microkinetic model employs a different sequestration mechanism from a previous microkinetic model for Zn-term ZnO(0001),[24] as well as a different charge state for O$_i$

and a statistical correction for temporary lattice sequestration, direct comparisons of between *F* require caution. However, a rough high-level comparison of diffusivities for the polar and nonpolar surfaces provides evidence for diffusional anisotropy in the bulk. D_{hop} for ZnO($10\bar{1}0$) along the *a* axis at 600 °C equals 2.4 × 10^{-8} cm^2 s^{-1} and the corresponding value for ZnO(0001) along the *c* axis equals 2.6 × 10^{-5} cm^2 s^{-1} – three orders of magnitude higher. Anisotropic O diffusion in ZnO has been reported due to dopants and impurities of the crystals in the literature in the slightly lower temperature range of 450–570°C, with *D* in the *c*-direction exceeding that in the *a*-direction by the same factor of 1000.[28]

2.3.2. Microkinetic model minus equilibrium assumption for [O_i]

One way to relax the assumption of O_i equilibrium between the surface and bulk assumes that the coverage θ of injectable species equilibrates with the gas phase but not with the bulk. As indicated in the main text, relaxation of the equilibrium assumption requires use of a different assumption to compute [O_i].

One possibility exploits the weak dependence of the profiles on *T* and P_{O_2}. This observation suggests the assumption that [S_U] remains approximately constant. [S_U] may then be lumped into an effective value for k_{asso} as a model output parameter. Relaxation of the equilibrium assumption permits the output parameter ΔH_f to be dropped from the set of parameters that require fitting.

Table S1 details the initial and optimized thermodynamic and kinetic parameters from the microkinetic model. The initial values originated mainly from an earlier version of the model for ZnO(0001)[24] or from educated guesses. Figure S5 shows an exemplary plot of an isotopic profile. In addition to the classical equilibrium results for *F* and D_{tr}, Figure S6 shows Arrhenius plots of these quantities obtained by combining the appropriate elementary parameters from the microkinetic model. Figure S7 displays the variation of the composite quantities with P_{O_2}. Table

S2 shows the effective activation energy and pre-exponential factor computed from the microkinetic parameters for *F* and D_{tr}, together with the exponent *b*.

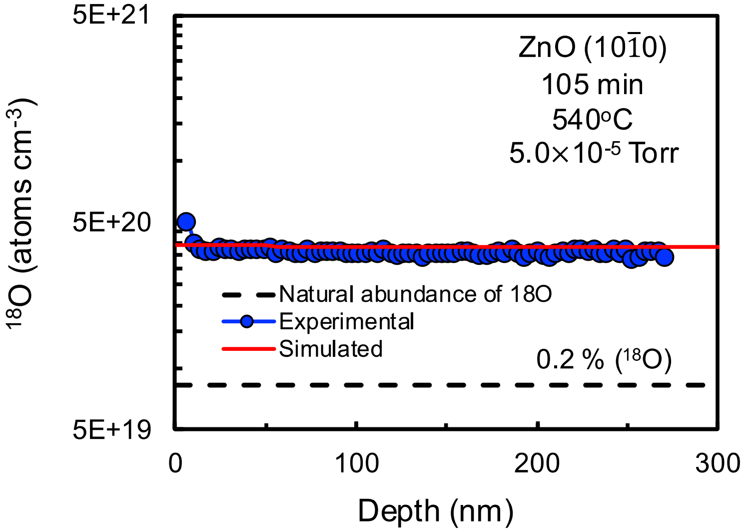

Figure S5. ^{18}O concentration profile (blue symbols) for nonpolar ZnO($10\bar{1}0$) with a representative microkinetic fit (solid red line) with relaxation of the equilibrium assumption for [O_i]. Dashed line represents the natural abundance ^{18}O concentration (0.2%) in ZnO.

Figures S6 and S7 show slight degradation in the quality of fitting to *F* and D_{tr} compared to those from the equilibrium model when compared to analytical-model parameters in the long-time limit. In particular, the values of *F* and D_{tr} from the modified microkinetic model overshoot rather consistently those from the analytical approach. This overshoot may result in part from the fact that uncertainties in the slopes and intercepts of the analytical approach propagate into *F* and D_{tr} in similar ways (Eqs. (S9) and (S10)), resulting in an artificially exaggerated compensation effect between them. The modified model does a much better job capturing the insensitivity of *F* to P_{O_2}, which is a notable weakness of the equilibrium model.

However, the sequestration energies seem unnaturally low, and the optimization loses sensitivity to certain other sequestration parameters (most notably *c*) – rendering their meaning obscure. The optimization remains sensitive to key parameters such as E_{inj}, S and E_{hop}, and returns the same value as the equilibrium model for E_{hop}. E_{inj} is slightly higher and matches the DFT value almost exactly. S_0 rises by several orders of magnitude, but n_{sat} declines by nearly the same amount to a value that does not cohere with the prediction from DFT that n_{sat} should have the same rough magnitude as the density of surface oxygen atoms. Since the mathematical product $n_{\mathrm{sat}}S_0$ is often difficult to deconvolve, the ability of the equilibrium assumption to accomplish the deconvolution represents a significant advantage. For purposes of comparison with DFT barriers for injection and hopping, either model probably suffices, but overall the equilibrium model offers somewhat better fits, does a better job with annihilation, and does not require exploitation of an *ad hoc* characteristic of the system such as weak T dependence.

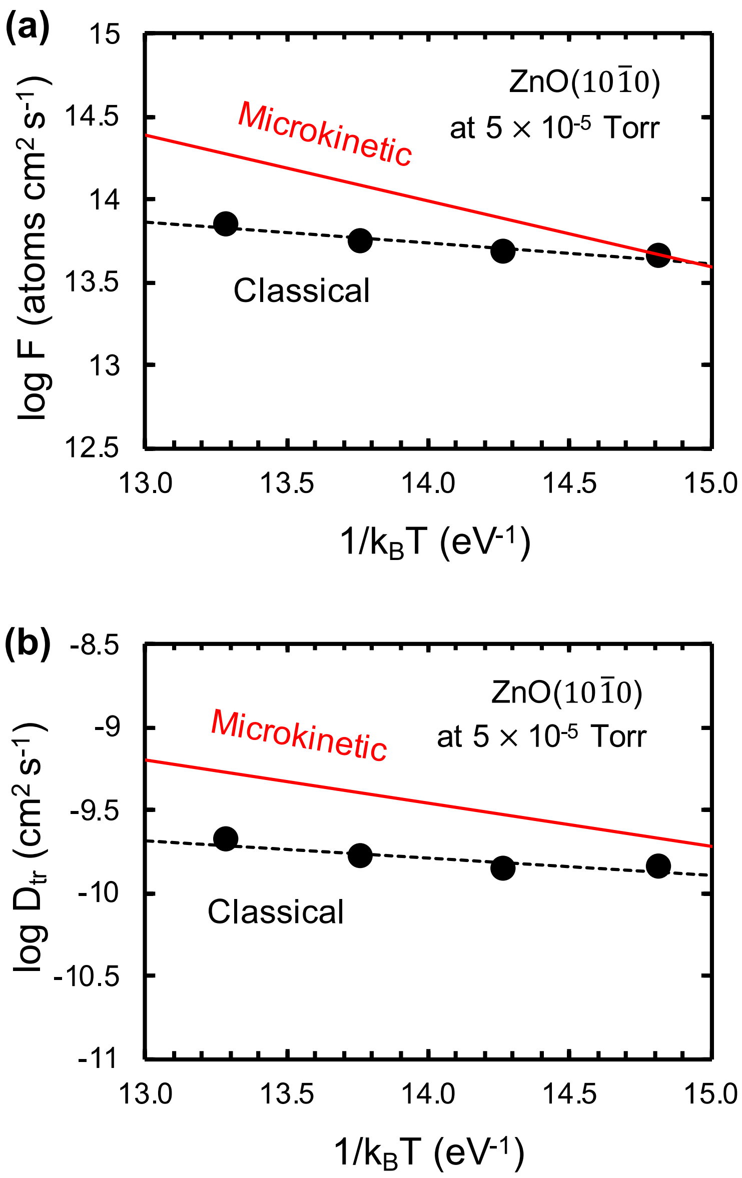

Figure S6. Arrhenius plots of (a) net injection flux *F* and (b) effective diffusivity D_{tr} for classical thermodynamic and microkinetic model at P_{O_2}= 5 × 10^{-5} Torr with relaxation of the equilibrium assumption for [O_i].

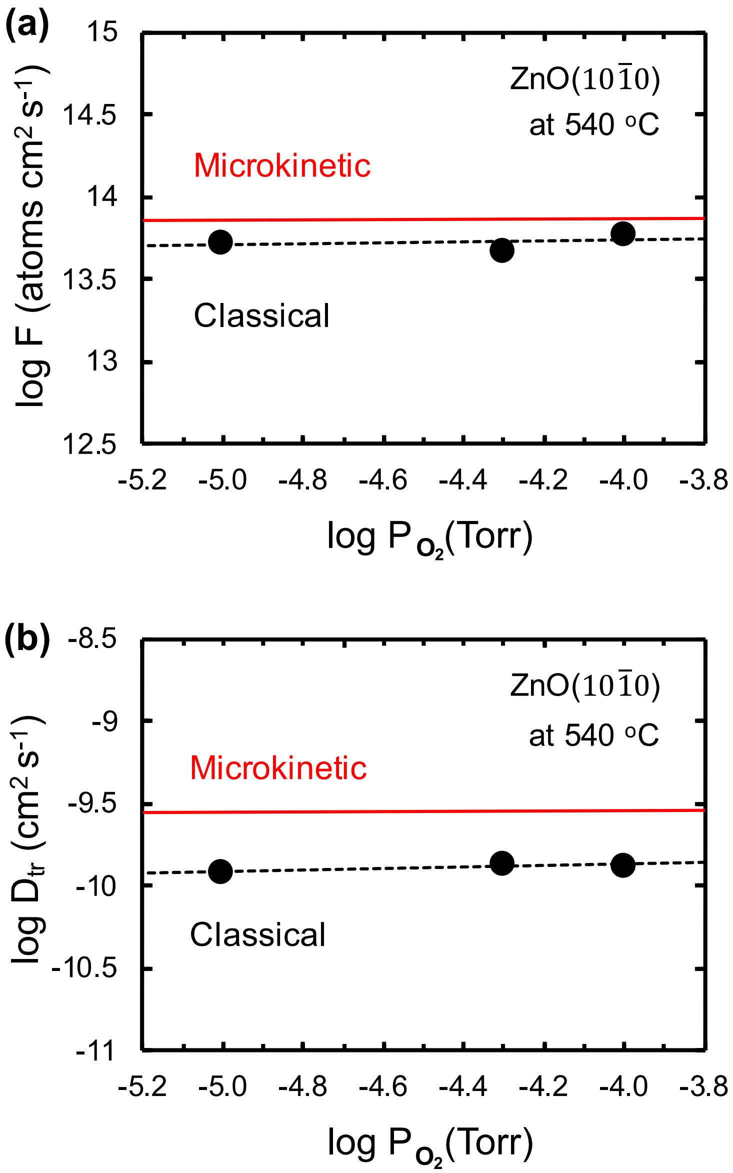

Figure S7. Oxygen partial pressure dependence of (a) *F* and (b) D_{tr} for classical thermodynamic and microkinetic models at $T = 540$ °C with relaxation of the equilibrium assumption for [O_i].

Table S1. Initial and final microkinetic parameters for microkinetic model with relaxation of the equilibrium assumption for [O_i].

Parameter	Definition	Initial value	Final estimate
ΔH_{fs}	effective formation enthalpy for sequestration sites	2.2 ± 0.2 eV	1.19 ± 0.1 eV
S_{tot}	effective formation prefactor for sequestration sites	$(6.13 \pm 0.6) \times 10^{36}$ atoms cm^{-3}	$(4.9 \pm 0.5) \times 10^{26}$ atoms cm^{-3}
c	effective pressure exponent in (P_{O_2}/P^0)^c for sequestration sites	0.45	0.45
E_{hop}	hopping barrier of bulk O_i	0.89 ± 0.08 eV	0.89 ± 0.08 eV
$D_{0,hop}$	hopping prefactor of bulk O_i	$(3.25 \pm 0.32) \times 10^{-3}$ cm^2 s^{-1}	$(3.58 \pm 0.3) \times 10^{-3}$ cm^2 s^{-1}
E_{diss}	barrier to liberate O_i from bulk defect complexes	1.6 ± 0.1 eV	1.2 ± 0.1 eV
A_{diss}	prefactor to liberate O_i from bulk defect complexes	$(1.0 \pm 0.1) \times 10^{13}$ s^{-1}	$(5.0 \pm 0.5) \times 10^{12}$ s^{-1}
E_{inj}	injection barrier	1.2 ± 0.1 eV	1.2 ± 0.1 eV
ν_{inj}	injection prefactor	$(1.0 \pm 0.1) \times 10^{10}$ s^{-1}	$(1.0 \pm 0.1) \times 10^{10}$ s^{-1}
n_{sat}	saturation concentration of injection sites	$(1.25 \pm 0.1) \times 10^{11}$ cm^{-2}	$(1.25 \pm 0.1) \times 10^{11}$ cm^{-2}
S_0	zero-coverage annihilation probability of O_i	$(6.0 \pm 0.6) \times 10^{-4}$	$(9.36 \pm 1.0) \times 10^{-3}$

Table S2. Components of composite parameters F and D_{tr} for microkinetic model with relaxation of the equilibrium assumption for [O$_i$]. Activation energies are given in eV. The units for pre-exponential factors of F and D_{tr} are cm^{-2} s^{-1} and cm^{2} s^{-1}, respectively.

Parameter	Activation energy / eV at P_{O_2}= 5×10^{-5} Torr		Pre-exponential factor at P_{O_2}= 5×10^{-5} Torr		Exponent b in $P_{O_2}^{b}$ at 540 °C	
	analytical	microkinetic	analytical	microkinetic	analytical	microkinetic
F	0.23 ± 0.05	0.92 ± 0.02	$1 \times 10^{(15.17 \pm 0.35)}$	$1 \times 10^{(45.08 \pm 0.37)}$	0.02 ± 0.09	1×10^{-4}
D_{tr}	0.13 ± 0.07	0.60 ± 0.02	$1 \times 10^{(-9.01 \pm 0.45)}$	$1 \times 10^{(-13.41 \pm 0.35)}$	0.03 ± 0.01	0.8×10^{-4}

3. References

1 H. C. Casey and G. L. Pearson, in *Point defects in solids*, Springer, 1975, pp. 163–255.

2 J. Maier, Mass transport in the presence of internal defect reactions—concept of conservative ensembles: I, chemical diffusion in pure compounds, *J. Am. Ceram. Soc.*, 1993, **76**, 1212–1217.

3 H. Schmidt, G. Borchardt, M. Rudolphi, H. Baumann, M. Bruns, S. Weber and H. Scherrer, in *Defect and Diffusion Forum*, Trans Tech Publ, 2005, vol. 237, pp. 512–517.

4 D. Shaw, in *Springer Handbook of Electronic and Photonic Materials*, Springer, 2017, p. 1.

5 J. Maier, Mass transport in the presence of internal defect reactions—Concept of conservative ensembles: IV, Tracer diffusion and intercorrelation with chemical diffusion and ion conductivity, *J. Am. Ceram. Soc.*, 1993, **76**, 1228–1232.

6 P. Erhart, K. Albe and A. Klein, First-principles study of intrinsic point defects in ZnO: Role of band structure, volume relaxation, and finite-size effects, *Phys. Rev. B*, 2006, **73**, 205203.

7 A. Janotti and C. G. Van de Walle, Native point defects in ZnO, *Phys. Rev. B*, 2007, **76**, 165202.

8 R. Vidya, P. Ravindran, H. Fjellvåg, B. G. Svensson, E. Monakhov, M. Ganchenkova and R. M. Nieminen, Energetics of intrinsic defects and their complexes in ZnO investigated by density functional calculations, *Phys. Rev. B*, 2011, **83**, 45206.

9 A. Goyal, P. Gorai, H. Peng, S. Lany and V. Stevanović, A computational framework for automation of point defect calculations, *Comput. Mater. Sci.*, 2017, **130**, 1–9.

10 H. Peng, First-principles study of native defects in rutile TiO 2, *Phys. Lett. A*, 2008, **372**, 1527–1530.

11 B. J. Morgan and G. W. Watson, Intrinsic n-type defect formation in TiO2: a comparison of rutile and anatase from GGA+ U calculations, *J. Phys. Chem. C*, 2010, **114**, 2321–2328.

12 H.-Y. Lee, S. J. Clark and J. Robertson, Calculation of point defects in rutile TiO2 by the screened-exchange hybrid functional, *Phys. Rev. B*, 2012, **86**, 75209.

13 E. G. Seebauer, K. Dev, M. Y. L. Jung, R. Vaidyanathan, C. T. M. Kwok, J. W. Ager, E. E. Haller and R. D. Braatz, Control of defect concentrations within a semiconductor through adsorption, *Phys. Rev. Lett.*, 2006, **97**, 55503.

14 P. Gorai, E. Ertekin and E. G. Seebauer, Surface-assisted defect engineering of point defects in ZnO, *Appl. Phys. Lett.*, 2016, **108**, 241603.

15 A. G. Hollister, P. Gorai and E. G. Seebauer, Surface-based manipulation of point defects in rutile TiO2, *Appl. Phys. Lett.*, 2013, **102**, 231601.

16 A. Claverie, B. Colombeau, G. Ben Assayag, C. Bonafos, F. Cristiano, M. Omri and B. de Mauduit, Thermal evolution of extended defects in implanted Si:: impact on dopant diffusion, *Mater. Sci. Semicond. Process.*, 2000, **3**, 269–277.

17 A. Claverie, F. Cristiano, B. Colombeau, E. Scheid and B. De Mauduit, in *Ion Implantation Technology. 2002. Proceedings of the 14th International Conference on*, IEEE, 2002, pp. 538–543.

18 K. L. Gilliard and E. G. Seebauer, Manipulation of native point defect behavior in rutile TiO2 via surfaces and extended defects, *J. Phys. Condens. Matter*, 2017, **29**, 445002.

19 J. Crank, *The mathematics of diffusion*, Oxford university press, 1979.

20 H. S. Carslaw and J. C. Jaeger, *Conduction of heat in solids*, Clarendon press, 1992.

21 N. E. B. Cowern, K. T. F. Janssen, G. F. A. Van de Walle and D. J. Gravesteijn, Impurity diffusion via an intermediate species: The B-Si system, *Phys. Rev. Lett.*, 1990, **65**, 2434.

22 R. Vaidyanathan, M. Y. L. Jung, R. D. Braatz and E. G. Seebauer, Measurement of defect-mediated diffusion: The case of silicon self-diffusion, *AIChE J.*, 2006, **52**, 366–370.

23 P. Gorai, A. G. Hollister and E. G. Seebauer, Measurement of defect-mediated oxygen self-diffusion in metal oxides, *ECS J. Solid State Sci. Technol.*, 2012, **1**, Q21–Q24.

24 M. Li and E. G. Seebauer, Microkinetic Model for Oxygen Interstitial Injection from the ZnO (0001) Surface into the Bulk, *J. Phys. Chem. C*, 2018, **122**, 2127–2136.

25 R. Gunawan, M. Y. L. Jung, R. D. Braatz and E. G. Seebauer, Parameter Sensitivity Analysis Applied to Modeling Transient Enhanced Diffusion and Activation of Boron in Silicon, *J. Electrochem. Soc.*, 2003, **150**, G758.

26 B. P. Uberuaga and X.-M. Bai, Defects in rutile and anatase polymorphs of TiO2: kinetics and thermodynamics near grain boundaries, *J. Phys. Condens. Matter*, 2011, **23**, 435004.

27 X.-M. Bai and B. P. Uberuaga, Multi-timescale investigation of radiation damage near TiO2 rutile grain boundaries, *Philos. Mag.*, 2012, **92**, 1469–1498.

28 H. Haneda, I. Sakaguchi, A. Watanabe, T. Ishigaki and J. Tanaka, Oxygen diffusion in single-and poly-crystalline zinc oxides, *J. Electroceramics*, 1999, **4**, 41–48.